Supplementary Information

Optical access of spin-polarized excited states in $Cs(PbMgZnCd)Br_3$ nanocrystals

Yu Zhang[1,2,†], Haidi Liu[1,2,†], Shuchun Zhang[1,2], Zhengwei Yang[1,2], Qingda Chang[1,2], Lixin Xu[1,2], Yongli Yan[1] and Chuang Zhang[1,]*

[1]Key Laboratory of Photochemistry, Beijing National Laboratory for Molecular Sciences, Institute of Chemistry, Chinese Academy of Sciences, Beijing 100190, China

[2]University of Chinese Academy of Sciences, Beijing 100049, China

*e-mail: zhangc@iccas.ac.cn.

†These authors contributed equally: Yu Zhang, Haidi Liu.

Contents

Figure S12 PL spectra of (a) $CsPbBr_3$ and (b) $Cs(PbMgZnCd)Br_3$ nanocrystals recorded under ambient conditions over a period of 10 days. (c) PL intensity as a function of storage time for $CsPbBr_3$ and $Cs(PbMgZnCd)Br_3$ nanocrystals.

Figure S13 Absorption spectra of $CsPbBr_3$ and $Cs(PbMgZnCd)Br_3$ nanocrystals.

Figure S14 PLQYs measured for (**a**) $CsPbBr_3$ and (**b**) $Cs(PbMgZnCd)Br_3$ nanocrystals.

Figure S15 Calculated band structures and DOS of $CsPbBr_3$.

Figure S16 Temperature-dependent PL spectra of (**a**) $CsPbBr_3$ and (**b**) $Cs(PbMgZnCd)Br_3$ (6-300 K) nanocrystals.

Figure S17 The fitted curve of temperature-dependent fluorescence FWHM for $CsPbBr_3$ and $Cs(PbMgZnCd)Br_3$ (6-300 K) nanocrystals.

Figure S18 The temperature-dependent PL decay dynamics of (a) $CsPbBr_3$ and (b) $Cs(PbMgZnCd)Br_3$ nanocrystals.

Figure S19 Calculated structural distortions for models with 1-2 doped metal species at the M-site.

Figure S20 (a) Schematic of a (101)-oriented monolayer of $[PbBr_6]^{4-}$ octahedra in $CsPbBr_3$. (b) Theoretical estimation of Rashba spin splitting in the band structure of $CsPbBr_3$.

Figure S21 (a) Schematic illustration of the device geometry for circular photogalvanic effect (CPGE) measurements. (b) Photocurrent measured from $Cs(PbMgZnCd)Br_3$ and $CsPbBr_3$ devices under alternating σ^+/σ^- light illumination at incident angles θ of +45° and -45°.

Figure S22 Schematic diagram of the circular polarization-dependent TA experimental setup.

Figure S23 The ground-state PB decay dynamics of $CsPbBr_3$ and $Cs(PbMgZnCd)Br_3$ nanocrystals at 500 nm.

Figure S24 Pump-probe TA spectra in $\sigma^+\sigma^+$ and $\sigma^+\sigma^-$ configurations at different delay times from 0 to 300 ps for (a) $CsPbBr_3$ and (b) $Cs(PbMgZnCd)Br_3$ nanocrystals.

Figure S25 PL spectra (a), PL lifetime (b) and spin relaxation time (c) of $CsPb_{1-x}Mg_xBr_3$ nanocrystals.

Figure S26 Schematic diagram of a circularly polarized injection and read-out experimental setup.

Figure S27 Schematic of the circularly spin-injected (σ^+) and polarized spin red-out of PL emission components, PL (σ^+) and PL (σ^-) in LHP.

Figure S28 Schematic set-up for measuring the optical Hanle effect.

Figure S29 Magneto-circular photoluminescence spectra of (a) Cs(PbMgZnCd)Br_3 and (c) $CsPbBr_3$ nanocrystal films. The magnetic field dependence of MCPL, from which the g-factor for the excitons in (b) Cs(PbMgZnCd)Br_3 and (d) $CsPbBr_3$.

Figure S30 The temperature-dependent Hanle curves of P_{PL} (B_z) response for $CsPbBr_3$ (a) and Cs(PbMgZnCd)Br_3 (b) nanocrystals.

Figure S31 Circularly polarized photoluminescence spectra at 6 K.

Figure S32 The B_z dependent PL intensity curves under $\sigma^+\sigma^+$ and $\sigma^+\sigma^-$ modes at 6 K.

Figure S33 Emission spectra from a Cs(PbMgZnCd)Br_3 nanocrystals under (a) right and (b) left circularly polarized excitation of different pump fluences.

Figure S34 The PL decay dynamics of Cs(PbMgZnCd)Br_3 nanocrystals under different pump fluences.

Figure S35 (a) Circularly polarized (σ^+ and σ^-) ASE under σ^+ laser pulses from $CsPbBr_3$. (b) The PL decay dynamics of $CsPbBr_3$ nanocrystals under pump fluences of 7.7 μJ cm^{-2}.

Figure S36 (a) Time-dependent plots of σ^+ and σ^- ASE intensities over 48 h at a σ^+ pump fluence of 6.5 μJ/cm^2 and corresponding *P* values from Cs(PbMgZnCd)Br_3. (b) ASE spectra at 0 h and 48 h.

Figure S37 (a) Circularly polarized (σ^+ and σ^-) ASE under σ^- laser pulses from Cs(PbMgZnCd)Br_3. (b) Plots of σ^+ and σ^- emission intensities versus σ^- pump fluences and corresponding P_{ASE} values from Cs(PbMgZnCd)Br_3.

Figure S38 Polarization angle-dependent profiles of ASE from Cs(PbMgZnCd)Br_3 nanocrystals under (a) σ^+ and (b) σ^- pump fluences.

Figure S39 The P_{ASE} modulation from Cs(PbMgZnCd)Br_3 by switching on-off B_z at 500 mT.

Table S1 | PL decay dynamics (λ_{ex} = 480 nm, pulsed width ~300 ps) recorded from $CsPbBr_3$ and $Cs(PbMgZnCd)Br_3$.

	ns	6 K	60 K	120 K	180 K	240 K	300 K
$CsPbBr_3$	τ_1 (A_1)	3.1 (84.6%)	3.4 (80.6%)	3.6 (80.1%)	3.7 (71.3%)	3.9 (60.8%)	4.1 (57.0%)
	τ_2 (A_2)	20.5 (15.4%)	21.1 (19.4%)	21.5 (19.9%)	21.8 (28.7%)	22.1 (39.2%)	23.2 (43.0%)
	τ_R	5.8	6.8	7.2	8.9	11.0	12.3
$Cs(PbMgZnCd)Br_3$	τ_1 (A_1)	2.3 (99.3%)	2.5 (99.0%)	2.6 (98.7%)	2.7 (98.2%)	3.0 (97.8%)	3.4 (97.0%)
	τ_2 (A_2)	21.6 (0.7%)	21.7 (1.0%)	22.5 (1.3%)	23.2 (1.8%)	24.3 (2.2%)	25.4 (3.0%)
	τ_R	2.4	2.7	2.9	3.1	3.5	4.1

Table S2 | Δd and σ^2 for $[PbBr_6]^{4-}$ octahedra in models with 1-4 metal species at the M-site.

M-site	Number of M	Δd (average)	σ^2 (average)
Pb	Monometallic	0	0.22
PbMg	Bimetallic	5.41×10^{-5}	5.22
PbZn		3.24×10^{-5}	4.43
PbCd		1.25×10^{-5}	3.14
PbMgZn	Trimetallic	6.10×10^{-4}	19.51
PbMgCd		4.21×10^{-4}	14.35
PbZnCd		2.15×10^{-4}	10.37
PbMgZnCd	Tetrametallic	3.15×10^{-3}	29.10

Table S3 | Summary of spin lifetime measured in perovskites.

Perovskites	Morphology	Spin lifetime	Refer.
$Cs(PbMgZnCd)Br_3$	NCs	59.8 ps	**This work**
$CsPbBr_3$	NCs	4.6 ps	**This work**
	NCs	4.4 ps	*ACS Energy Lett.* **2022**, *7*, 4325–4332
	QDs	1.2 ps	*Nat. Nanotechnol.* **2023**, *18*, 124–130
	Film	3.8 ps	*J. Phys. Chem. Lett.* **2020**, *11*, 1502–1507
	Bulk	3.2 ps	*Sci. Adv.* **2020**, *6*, eabb7132
$MAPbBr_3$	SC	3.1 ps	*J. Phys. Chem. Lett.* **2018**, *9*, 2595–2603
	Film	4.3 ps	*J. Phys. Chem. Lett.* **2020**, *11*, 1502–1507
	Film	3.5 ps	*J. Phys. Chem. Lett.* **2018**, *9*, 2595–2603
$CsPbI_3$	NCs	3.9 ps	*Science* **2021**, *371*, 1129-1133
	QDs	3.2 ps	*ACS Energy Lett.* **2020**, *5*, 1701–1708
	2D NPs	0.9 ps	*Sci. Adv.* **2020**, *6*, eabb7132
	Film	3.2 ps	*Sci. Adv.* **2020**, *6*, eabb7132
	Film	2.2 ps	*J. Phys. Chem. Lett.* **2020**, *11*, 1502–1507
$MAPbI_3$	SC	1.5 ps	*ACS Energy Lett.* **2018**, *3*, 2273–2279
	Film	1.37 ps	*J. Phys. Chem. Lett.* **2018**, *9*, 2595–2603
	Film	2.2 ps	*J. Phys. Chem. Lett.* **2020**, *11*, 1502–1507
	Film	4 ps	*Nano Lett.* **2015**, *15*, 1553–1558
$CsSnBr_3$	NCs	18.0 ps	*ACS Energy Lett.* **2021**, *6*, 1670–1676
$MAPbIBr_2$	Film	3.3 ps	*J. Phys. Chem. Lett.* **2020**, *11*, 1502–1507
$MAPbI_2Br$	Film	2.3 ps	*J. Phys. Chem. Lett.* **2020**, *11*, 1502–1507
$CsPb(Br_{0.1}I_{0.9})_3$	NCs	14.2 ps	*Science* **2021**, *371*, 1129-1133
$BA_2FAPb_2I_7$	Film	3.2 ps	*Nano Lett.* **2020**, *20*, 5678–5685
$(EIA)_2(MA)_{n-1}PbnI_{3n+1}$	2D film	1.6 ps (n=1) 15.2 ps (n=2)	*Angew. Chem. Int. Ed.* **2023**, *62*, e202304486
$PEA_2PbI_4{\cdot}(MAPbI_3)_{n-1}$	SC	0.3 ps (n=1) 3.0 ps (n=2) 3.2 ps (n=3) 7.0 ps (n=4)	*ACS Energy Lett.* **2018**, *3*, 2273–2279

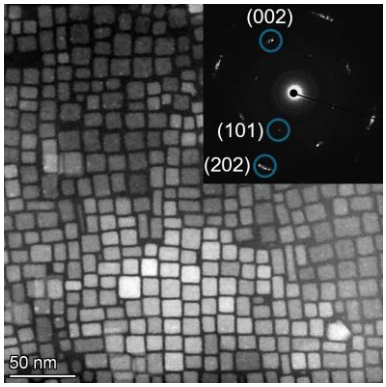

Fig. S1 | TEM images and SAED patterns for $CsPbBr_3$ nanocrystals. Scale bars: 50 nm for TEM images and 2 nm^{-1} for SAED patterns.

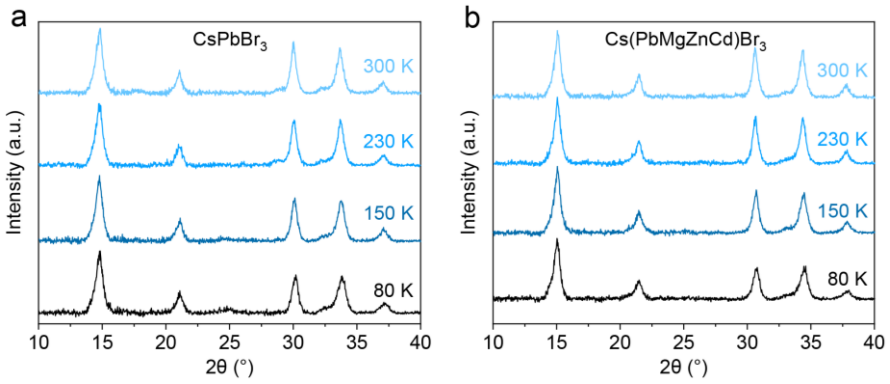

Fig. S2 | Temperature-dependent XRD patterns of $CsPbBr_3$ and $Cs(PbMgZnCd)Br_3$ nanocrystals recorded under different temperatures (300-80 K). The results show no obvious changes in diffraction patterns in a wide temperature range.

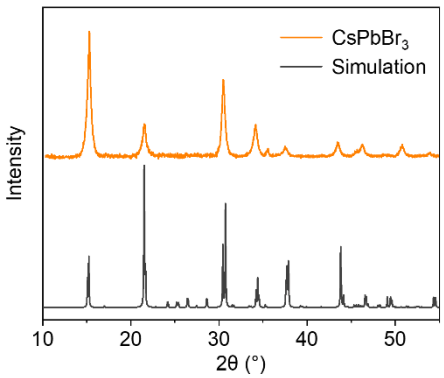

Fig. S3 | Experimental and simulated powder XRD patterns of $CsPbBr_3$ nanocrystals.

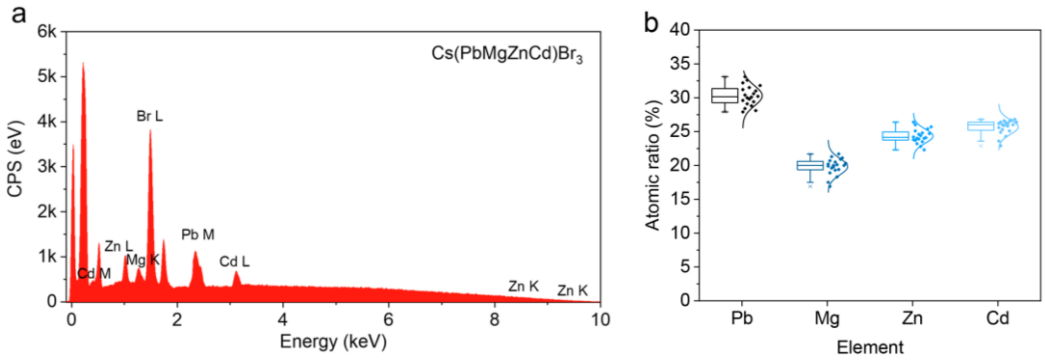

Fig. S4 | (a) Representative SEM-EDS spectrum of $Cs(PbMgZnCd)Br_3$ nanocrystals, showing the characteristic X-ray peaks of Pb, Mg, Zn, Cd, and Br. (b) distributions of Pb, Mg, Zn, and Cd atomic ratios obtained from SEM-EDS measurements. It shows that the composition of high-entropy perovskite nanocrystals is highly reproducible, and the distributions on elemental compositions (Pb ~30%, Mg ~20%, Zn ~24%, and Cd ~26%) are very narrow. The thermodynamically favored product is supposed to be governed by the interplay between configurational entropy and the solubility of MBr_2 salts during the ion-exchange process.

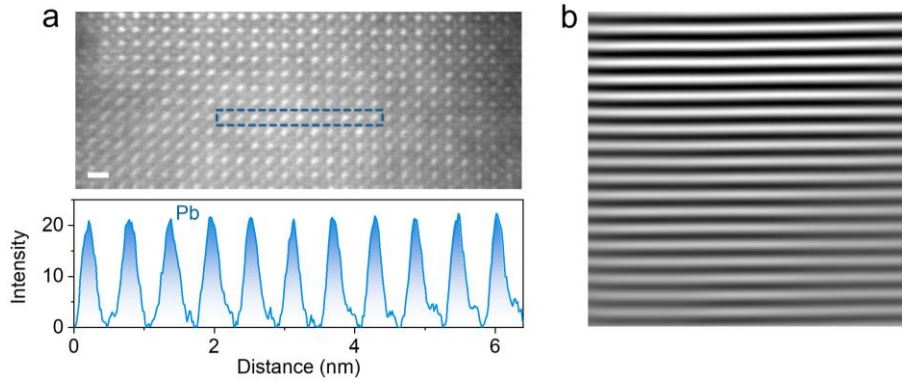

Fig. S5 | (a) Zoomed-in HAADF-TEM image of $CsPbBr_3$ nanocrystals, and corresponding intensity profiles in the region of blue dashed line. The scale bar is 1 nm. (b) Atomic inverse fast Fourier transform filtered image derived from the HRTEM images of $CsPbBr_3$.

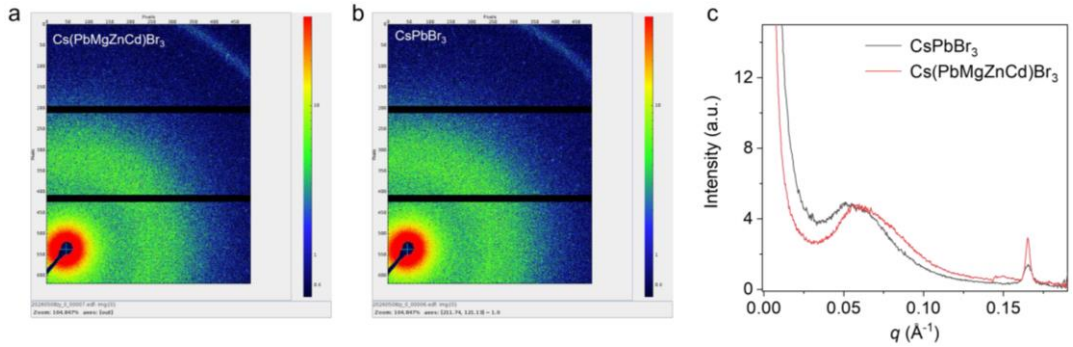

Fig. S6 | Two-dimensional SAXS patterns of (a) $Cs(PbMgZnCd)Br_3$ and (b) $CsPbBr_3$ nanocrystal films. (c) Corresponding azimuthally integrated one-dimensional SAXS profiles. The scattering feature at $q \sim 0.165$ Å^{-1} indicates that ordered structures are preserved upon high-entropy alloying. Broad features in the $q = 0.025$-0.100 Å^{-1} region may be related to the size of nanocrystals or internal domains; however, no clear quantitative difference can be resolved within the current SAXS resolution. This is because the size and spatial distribution of $[PbBr_6]^{4-}$ domains are highly random, and the SAXS signal may also be affected by disordered nanocrystal packing in the film.

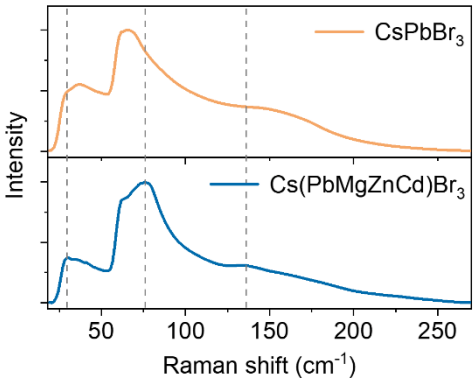

Fig. S7 | Raman spectra of $CsPbBr_3$ and $Cs(PbMgZnCd)Br_3$ nanocrystals.

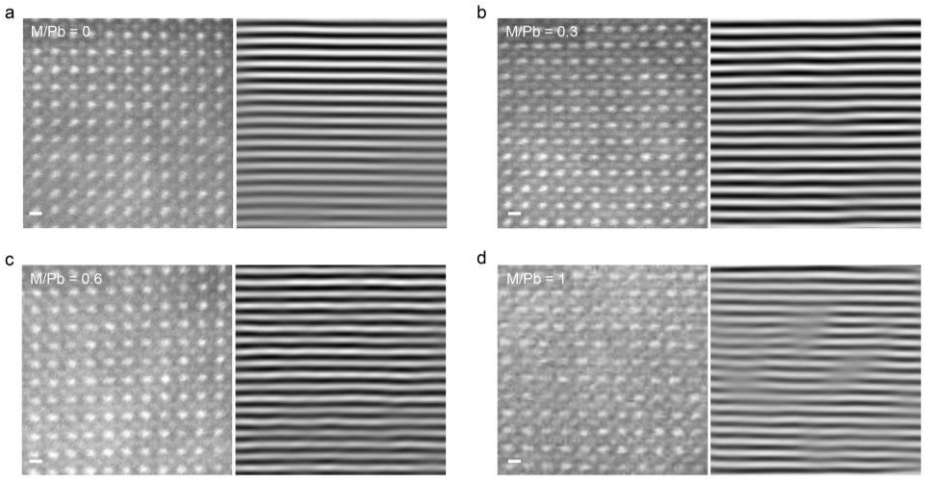

Fig. S8 | Atomic inverse fast Fourier transform filtered image derived from the HRTEM images of high-entropy LHPs with various M/Pb ratios. The lattice distortion and confinement can be observed upon the high-entropy doping in perovskite structures.

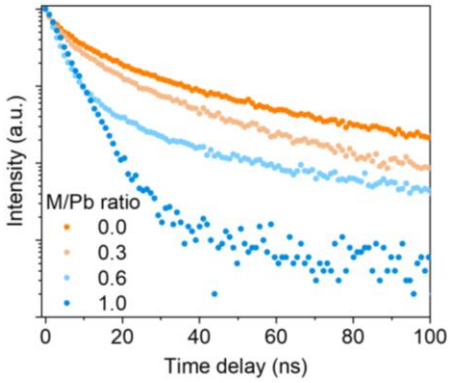

Fig. S9 | PL decay dynamics measured for the high-entropy LHPs with various M/Pb ratios.

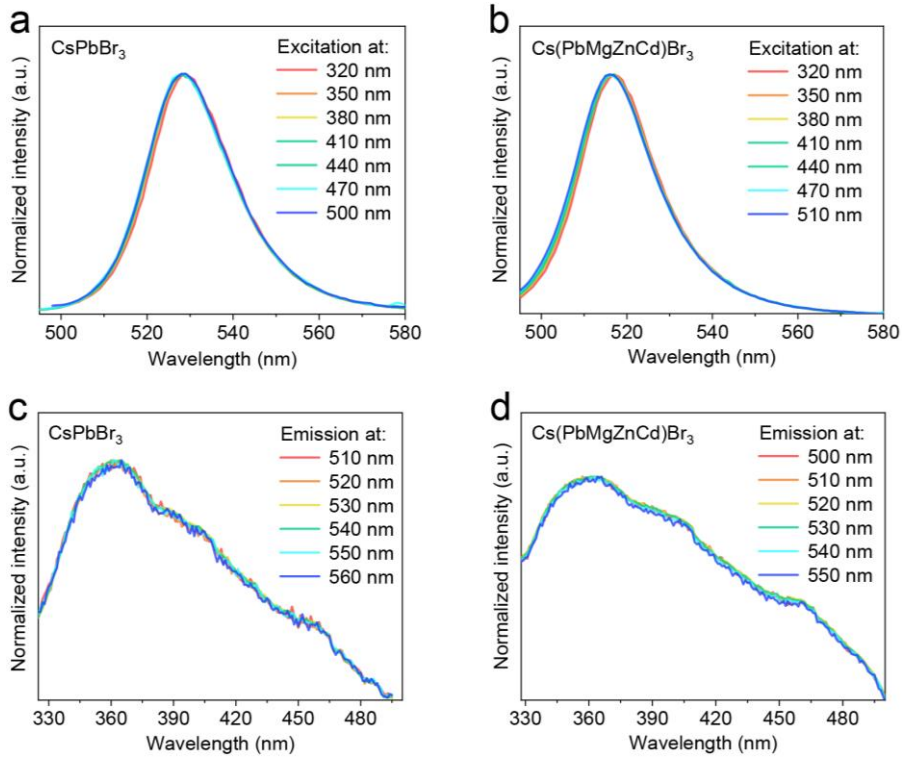

Fig. S10 | The excitation and emission spectra of $CsPbBr_3$ and $Cs(PbMgZnCd)Br_3$ nanocrystals measured at different wavelengths.

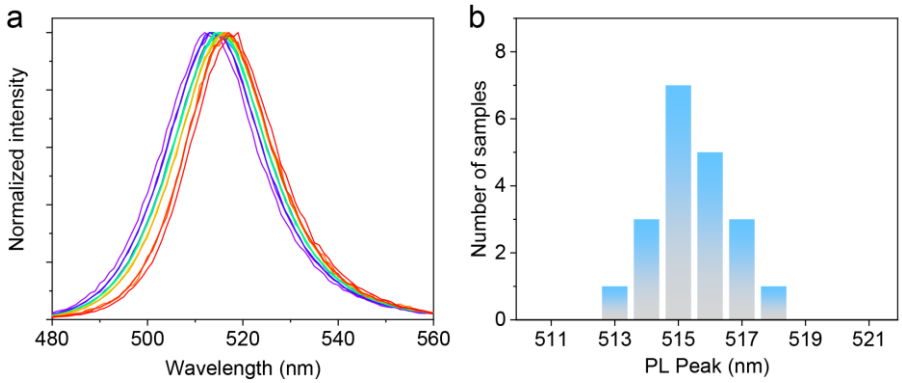

Fig. S11 | Statistical analysis of 20 parallel samples of $Cs(PbMgZnCd)Br_3$: (a) PL spectra; (b) the distribution of PL peak.

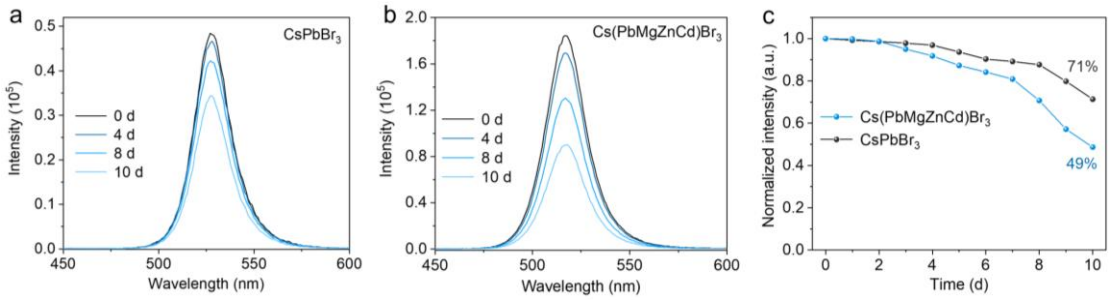

Fig. S12 | PL spectra of (a) $CsPbBr_3$ and (b) $Cs(PbMgZnCd)Br_3$ nanocrystals recorded under ambient conditions over a period of 10 days. (c) PL intensity as a function of storage time for $CsPbBr_3$ and $Cs(PbMgZnCd)Br_3$ nanocrystals. The two samples show comparable decay curves, and the decomposition of $Cs(PbMgZnCd)Br_3$ appears slightly more sensitive to moisture/oxygen than that of $CsPbBr_3$ over extended periods.

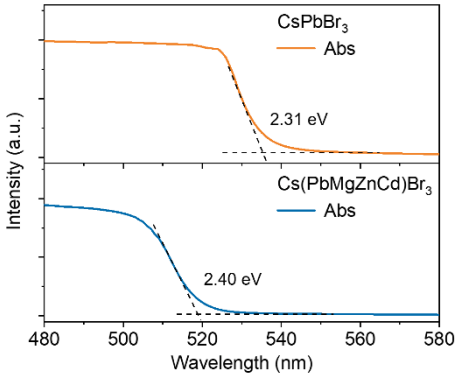

Fig. S13 | Absorption spectra of $CsPbBr_3$ and $Cs(PbMgZnCd)Br_3$ nanocrystals.

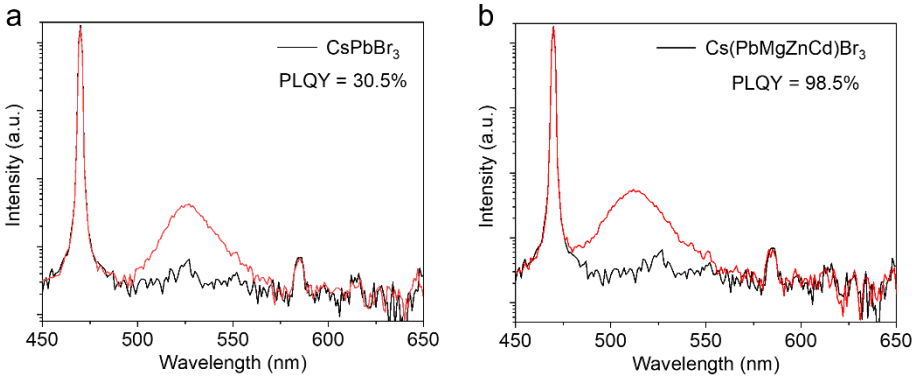

Fig. S14 | PLQYs measured for (a) $CsPbBr_3$ and (b) $Cs(PbMgZnCd)Br_3$ nanocrystals. The red and black plots are the raw emission spectra of the sample and the background (system dark and stray light signals) recorded under the same conditions in the integrating-sphere setup used for the PLQY measurements.

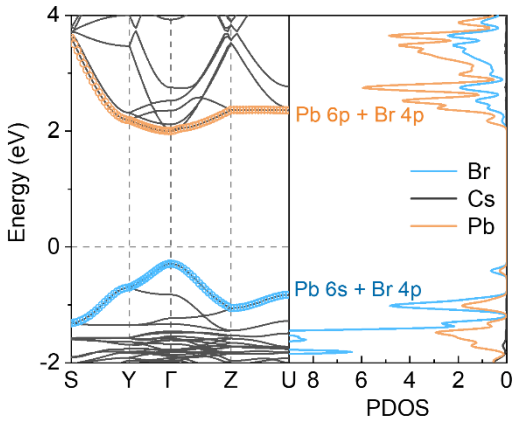

Fig. S15 | Calculated band structures and DOS of $CsPbBr_3$. The band structure is obtained by the Tran-Blaha modified Becke-Johnson (TB-mBJ) method without considering the contribution of SOC.

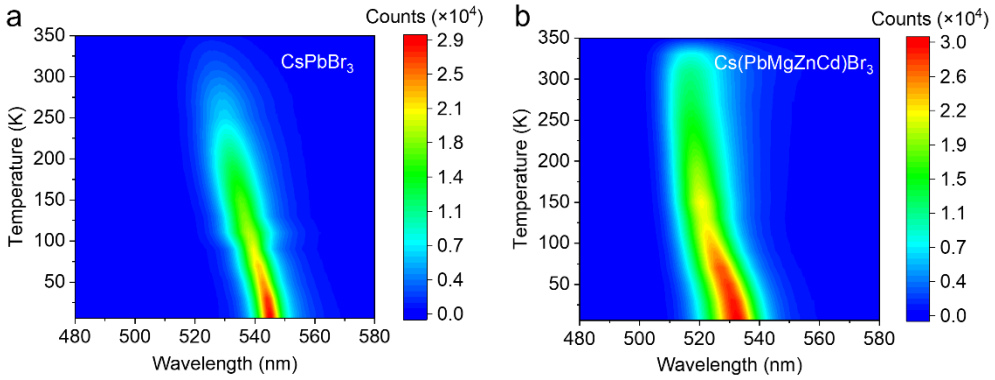

Fig. S16 | Temperature-dependent PL spectra of (a) $CsPbBr_3$ and (b) $Cs(PbMgZnCd)Br_3$ (6-300 K) nanocrystals.

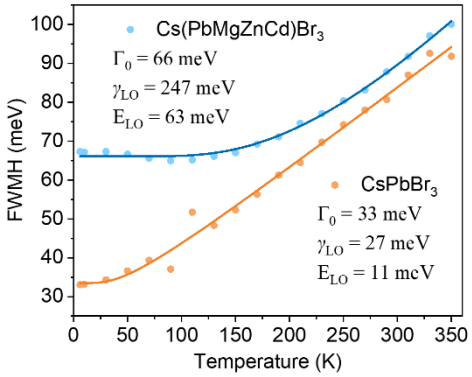

Fig. S17 | The fitted curve of temperature-dependent fluorescence FWHM for $CsPbBr_3$ and $Cs(PbMgZnCd)Br_3$ (6-300 K) nanocrystals. The curves represent the fitting results of the exciton-phonon coupling model.

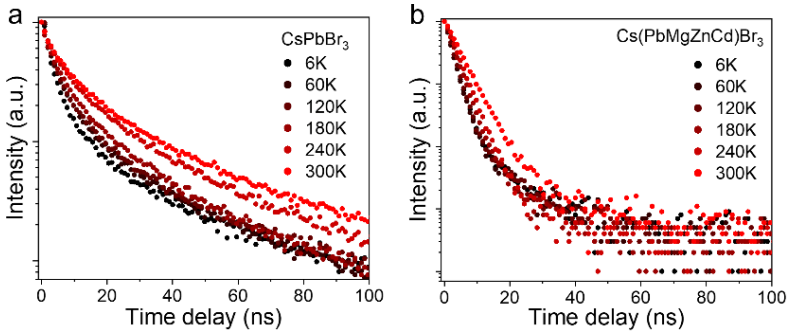

Fig. S18 | The temperature-dependent PL decay dynamics of (a) $CsPbBr_3$ and (b) $Cs(PbMgZnCd)Br_3$ nanocrystals.

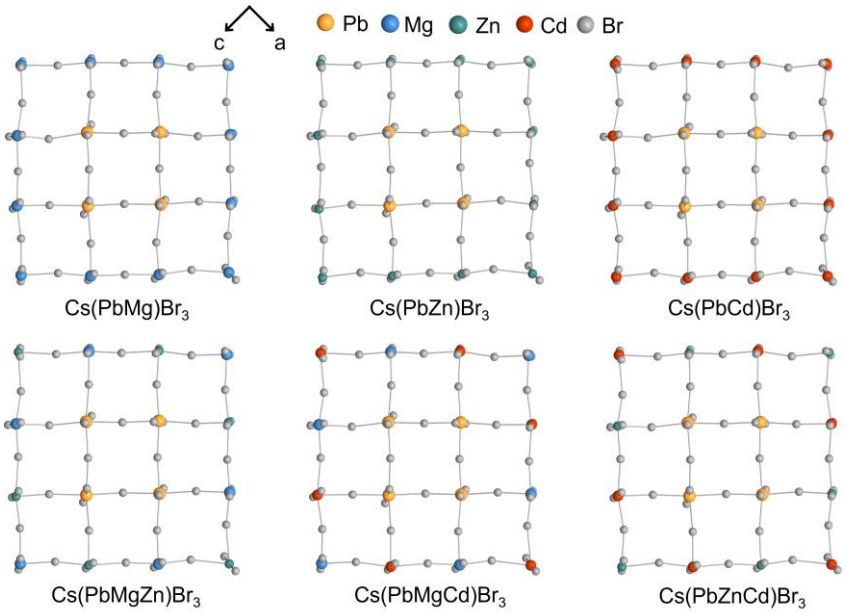

Fig. S19 | Calculated structural distortions for models with 1-2 doped metal species at the M-site. Doped metals with ionic radii that differ more from that of Pb tend to cause stronger lattice distortions, following the trend: Mg > Zn > Cd. More importantly, increasing the variety of doped metal species significantly intensifies lattice distortion, as the coexistence of multiple metals induces pronounced local spatial asymmetry.

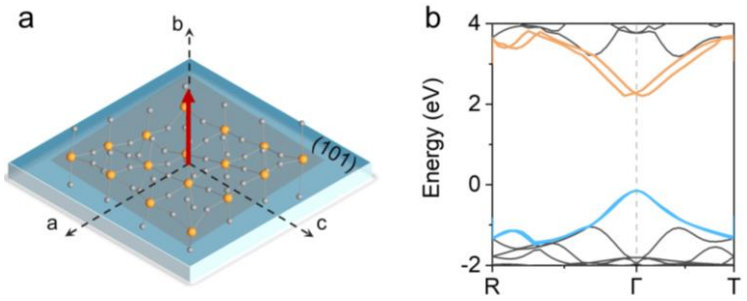

Fig. S20 | (a) Schematic of a (101)-oriented monolayer of $[PbBr_6]^{4-}$ octahedra in $CsPbBr_3$. (b) Theoretical estimation of Rashba spin splitting in the band structure of $CsPbBr_3$. The results are calculated by the Heyd-Scuseria-Ernzerhof (HSE06) hybrid functional method and SOC is taken into account within the first-principles framework as implemented in the VASP code. The inversion-symmetry breaking is perpendicular to the interface (red arrow), i.e., along the out-of-plane direction, and the Rashba splitting is expected to be pronounced within the plane of the (101)-oriented monolayer, i.e., the Γ-R and Γ-T paths in the orthorhombic Brillouin zone.

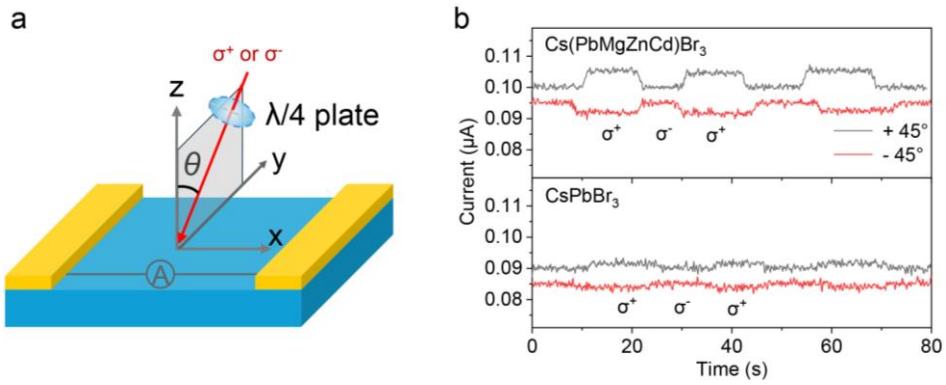

Fig. S21 | (a) Schematic illustration of the device geometry for circular photogalvanic effect (CPGE) measurements. (b) Photocurrent measured from $Cs(PbMgZnCd)Br_3$ and $CsPbBr_3$ devices under alternating σ^+/σ^- light illumination at incident angles θ of +45° and -45°. The nanocrystals were mixed with poly(vinylcarbazole) in the precursor solution, which was spin coated on interdigitated Au electrodes prepatterned on the substrate. The photocurrent is transverse to the plane of the incident laser to ensure the spin-momentum locking in the Rashba state. Under σ^+/σ^- light illumination by manually rotating the quarter-wave plate, the change of photocurrent is observed for both $CsPbBr_3$ and $Cs(PbMgZnCd)Br_3$ devices, and the sign of CPGE inverts when the angle of the laser incidence is reversed. The average CPGE values for $CsPbBr_3$ and $Cs(PbMgZnCd)Br_3$ are ~2.8% and ~1.1%, respectively, which further validates the presence of the Rashba effect in high-entropy nanocrystals.

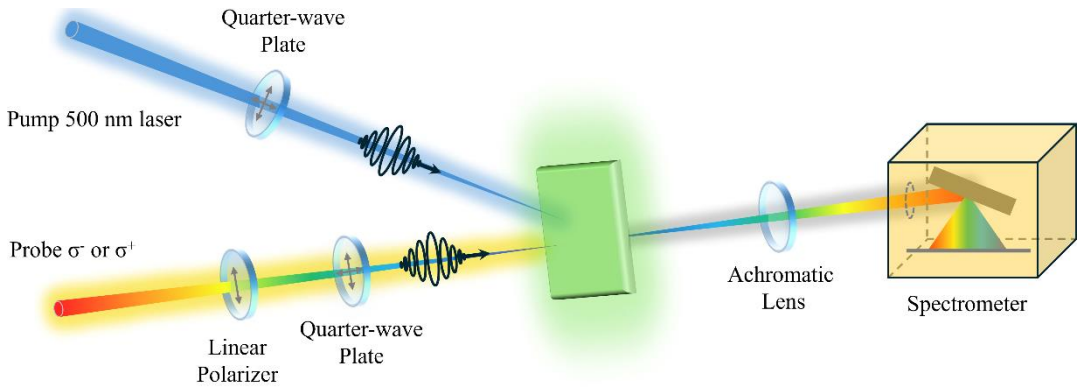

Fig. S22 | Schematic diagram of the circular polarization-dependent TA experimental setup.

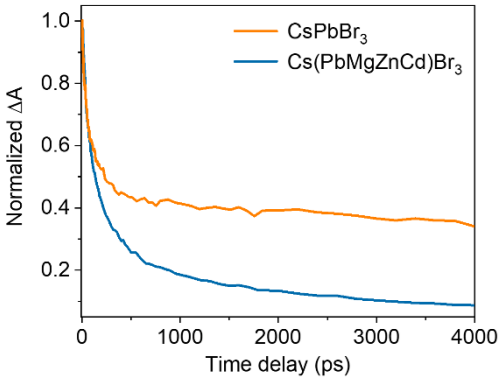

Fig. S23 | The ground-state PB decay dynamics of $CsPbBr_3$ and $Cs(PbMgZnCd)Br_3$ nanocrystals at 500 nm.

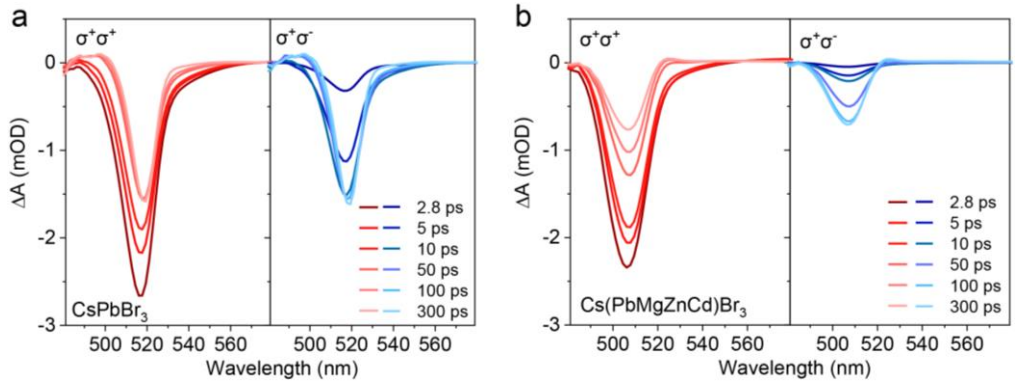

Fig. S24 | Pump-probe TA spectra in $\sigma^+\sigma^+$ and $\sigma^+\sigma^-$ configurations at different delay times from 0 to 300 ps for (a) $CsPbBr_3$ and (b) $Cs(PbMgZnCd)Br_3$ nanocrystals.

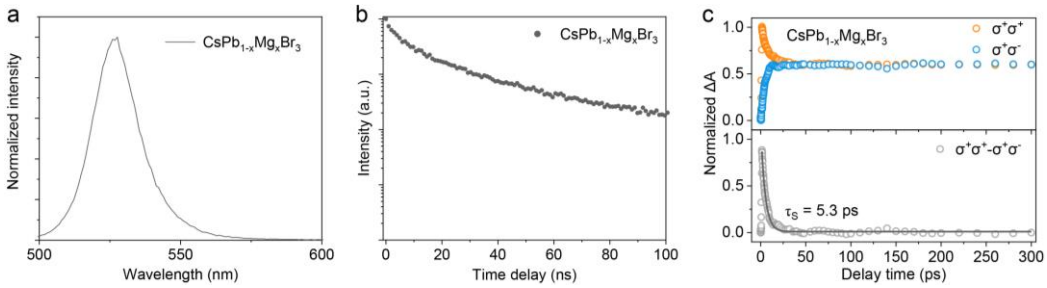

Fig. S25 | PL spectra (a), PL lifetime (b) and spin relaxation time (c) of $CsPb_{1-x}Mg_xBr_3$ nanocrystals. In $CsPb_{1-x}Mg_xBr_3$, we measured only a trace amount of Mg dopant in the "single-metal doping" $CsPbBr_3$, where x is ~0.012 according to inductively coupled plasma analysis.

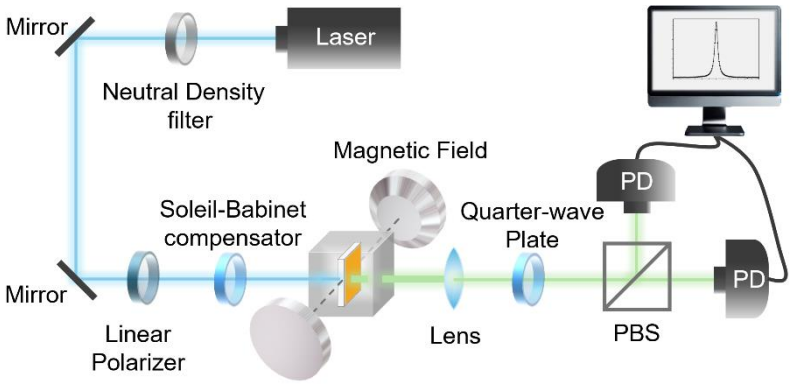

Fig. S26 | Schematic diagram of a circularly polarized injection and read-out experimental setup.

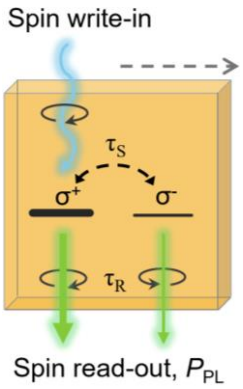

Fig. S27 | Schematic of the circularly spin write-in (σ^+) and polarized spin red-out of PL emission components, PL (σ^+) and PL (σ^-) in LHP. The spin relaxation process couples the two exciton states, with a spin lifetime τ_S.

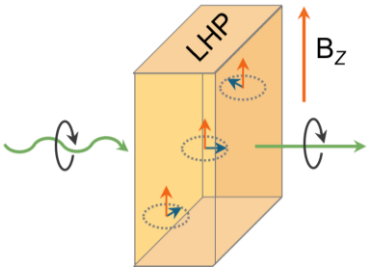

Fig. S28 | Schematic set-up for measuring the optical Hanle effect. A magnetic field, B_z perpendicular to the PL light propagation direction is applied, which causes spin precession that leads to diminishing circular polarization of PL.

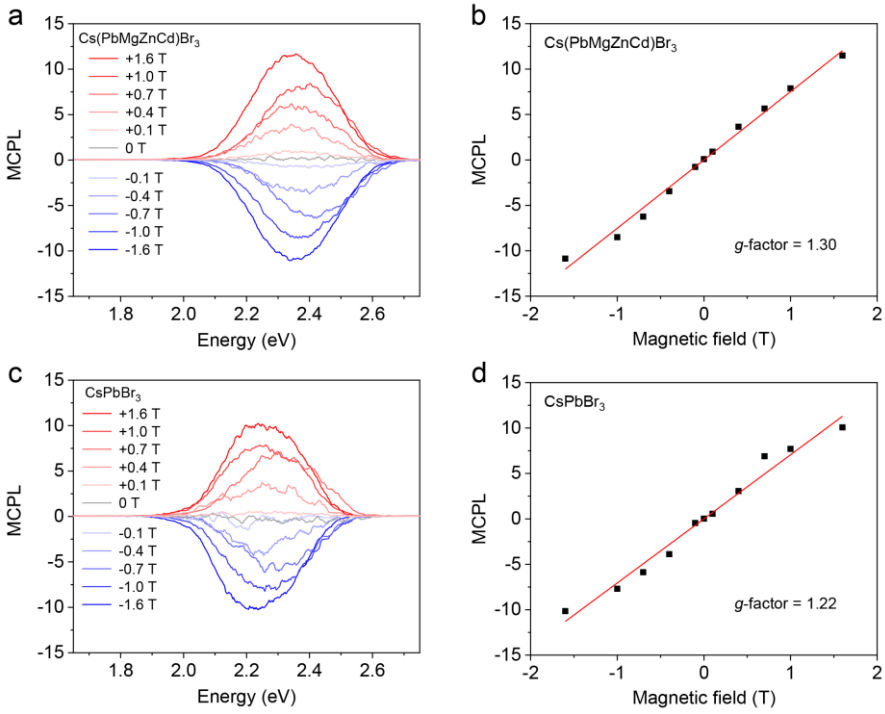

Fig. S29 | Magneto-circular photoluminescence spectra of (a) $Cs(PbMgZnCd)Br_3$ and (c) $CsPbBr_3$ nanocrystal films. The magnetic field dependence of MCPL, from which the g-factor for the excitons in (b) $Cs(PbMgZnCd)Br_3$ and (d) $CsPbBr_3$ were extracted using equation $\mathrm{MCPL(B)} = \frac{g_{ex}\mu_B B}{2k_B T}$.

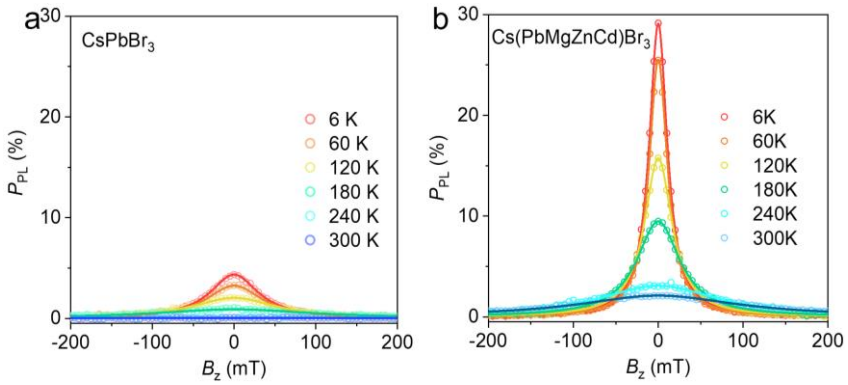

Fig. S30 | The temperature-dependent Hanle curves of P_{PL} (B_z) response for $CsPbBr_3$ (a) and $Cs(PbMgZnCd)Br_3$ (b) nanocrystals.

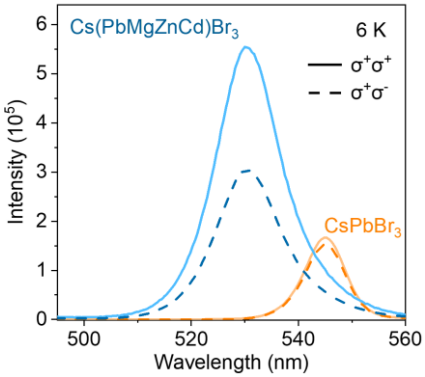

Fig. S31 | Circularly polarized photoluminescence spectra at 6K.

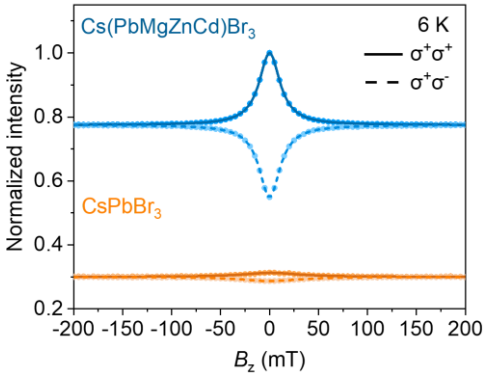

Fig. S32 | The B_z dependent PL intensity curves under $\sigma^+\sigma^+$ and $\sigma^+\sigma^-$ modes at 6 K.

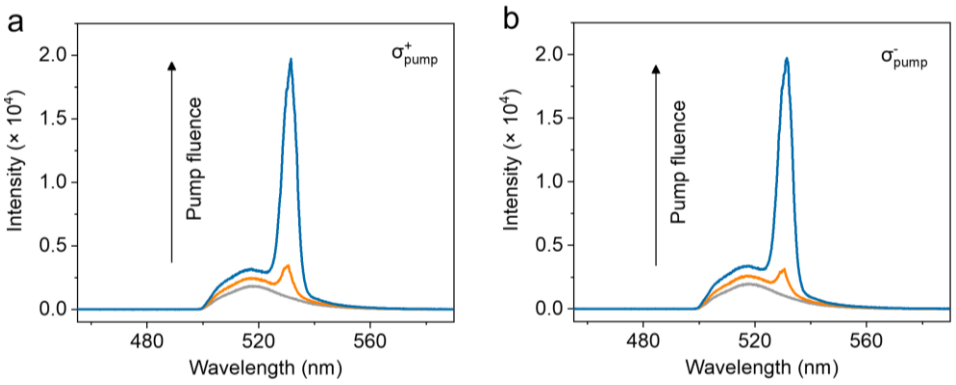

Fig. S33 | Emission spectra from a Cs(PbMgZnCd)Br_3 nanocrystals under (a) right and (b) left circularly polarized excitation of different pump fluences.

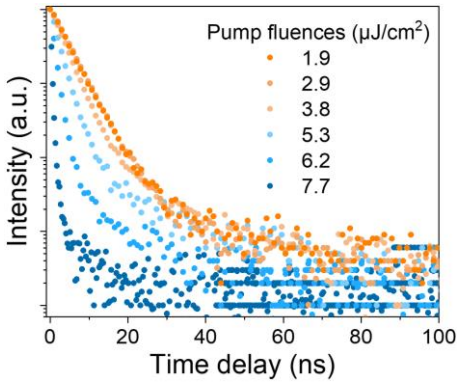

Fig. S34 | The PL decay dynamics of Cs(PbMgZnCd)Br_3 nanocrystals under different pump fluences.

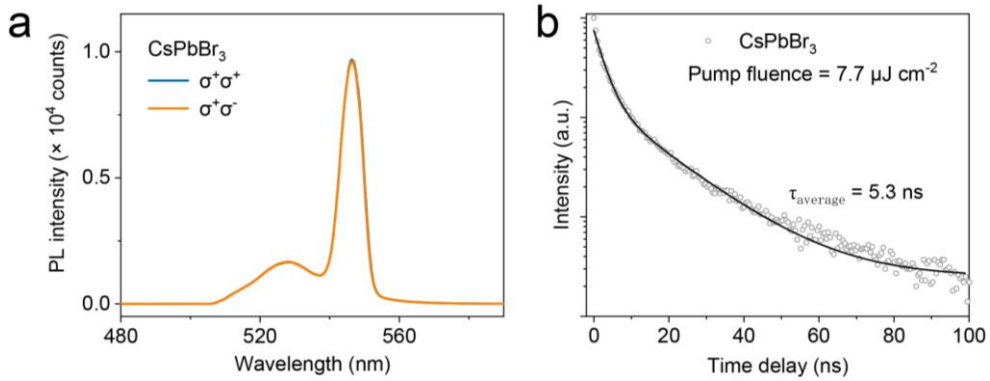

Fig. S35 | (a) Circularly polarized (σ^+ and σ^-) ASE under σ^+ laser pulses (λ_{ex} = 480 nm) from $CsPbBr_3$ (pump fluence = 7.7 μJ cm^{-2}). (b) The PL decay dynamics of $CsPbBr_3$ nanocrystals under pump fluences of 7.7 μJ cm^{-2}.

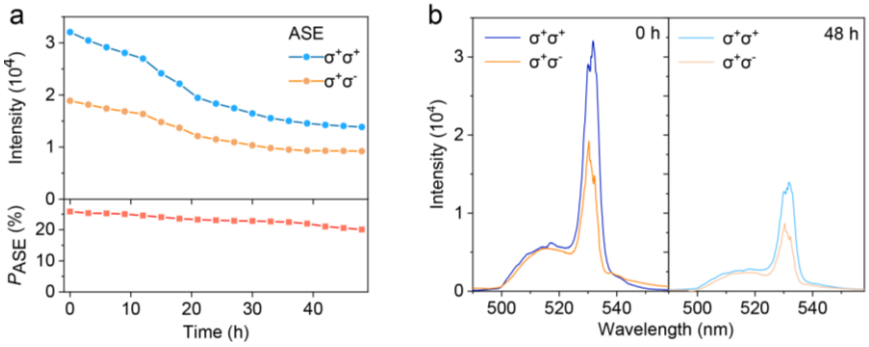

Fig. S36 | (a) Time-dependent plots of σ^+ and σ^- ASE intensities over 48 h at a σ^+ pump fluence of 6.5 μJ/cm^2 and corresponding *P* values from $Cs(PbMgZnCd)Br_3$. (b) ASE spectra at 0 h and 48 h.

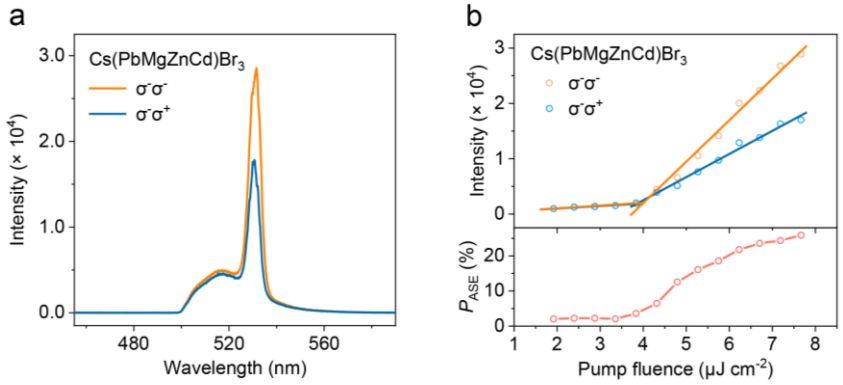

Fig. S37 | (a) Circularly polarized (σ^+ and σ^-) ASE under σ^- laser pulses (λ_{ex} = 480 nm) from $Cs(PbMgZnCd)Br_3$. (b) Plots of σ^+ and σ^- emission intensities versus σ^- pump fluences and corresponding P_{ASE} values from $Cs(PbMgZnCd)Br_3$.

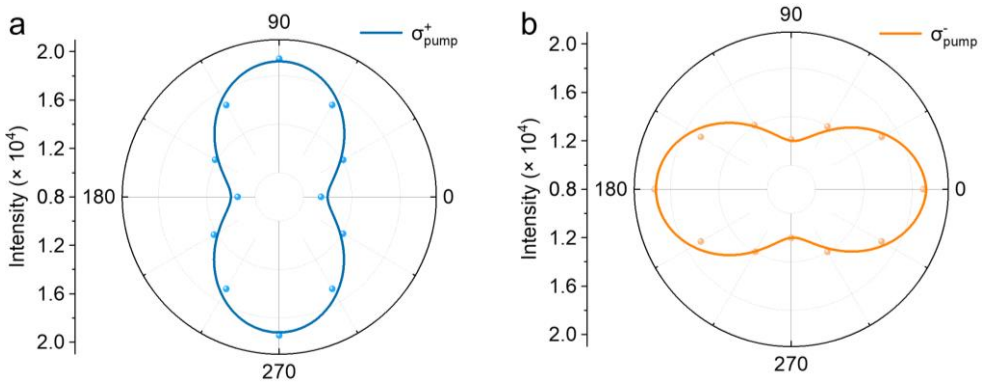

Fig. S38 | Polarization angle-dependent profiles of ASE from $Cs(PbMgZnCd)Br_3$ nanocrystals under (a) σ^+ and (b) σ^- pump fluences.

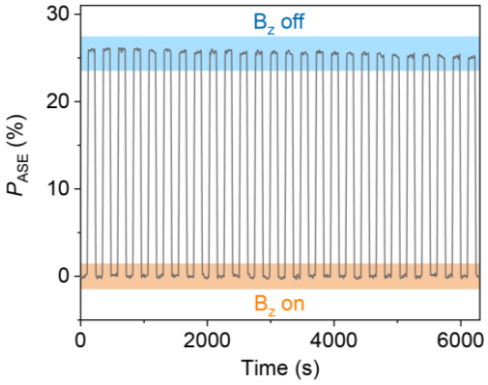

Fig. S39 | The P_{ASE} modulation from Cs(PbMgZnCd)Br_3 by switching on-off B_z at 500 mT.